

A year-round satellite sea ice thickness record from CryoSat-2

Jack C. Landy^{1,2*}, Geoffrey J. Dawson², Michel Tsamados³, Mitchell Bushuk⁴, Julienne C. Stroeve^{3,5}, Stephen E. L. Howell⁶, Thomas Krumpen⁷, David G. Babb⁵, Alexander S. Komarov⁸, Harry D. B. S. Heorton³, H. Jakob Belter⁷, Yevgeny Aksenov⁹

¹ Centre for Integrated Remote Sensing and Forecasting for Arctic Operations, Department of Physics and Technology, University of Tromsø: The Arctic University of Norway, Norway.

² Bristol Glaciology Centre, School of Geographical Sciences, University of Bristol, Bristol BS8 1SS, U.K.

³ Centre for Polar Observation and Modelling, Department of Earth Sciences, University College London, U.K.

⁴ National Oceanic and Atmospheric Administration/Geophysical Fluid Dynamics Laboratory, Princeton, New Jersey, U.S.A.

⁵ Centre for Earth Observation Science, University of Manitoba, Winnipeg, Manitoba, Canada.

⁶ Environment and Climate Change Canada, Climate Research Division, Toronto, Ontario, Canada.

⁷ Alfred Wegener Institute, Helmholtz Centre for Polar and Marine Research, Bremerhaven, Germany.

⁸ Environment and Climate Change Canada, Meteorological Research Division, Ottawa, Canada.

⁹ Marine Systems Modelling Group, National Oceanography Centre, European Way, Southampton, UK.

* Corresponding Author: Jack Landy, Email: jack.c.landy@uit.no

18 **Abstract**

19 Arctic sea ice is diminishing with climate warming¹ at a rate unmatched for at least 1000 years². As the receding
20 ice pack raises commercial interest in the Arctic³, it has become more variable and mobile⁴ which increases safety
21 risks to maritime users⁵. Satellite observations of sea ice thickness are currently unavailable during the crucial
22 melt period from May to September, when they would be most valuable for applications such as seasonal
23 forecasting⁷, owing to major challenges in the processing of altimetry data⁸. Here we use deep learning and
24 numerical simulations of the CryoSat-2 radar altimeter response to overcome these challenges and generate the
25 first pan-Arctic sea ice thickness dataset during the Arctic melt period. CryoSat-2 observations capture spatial and
26 temporal patterns of ice melting rates recorded by independent sensors and match the time series of sea ice volume
27 modelled by the Pan-Arctic Ice Ocean Modeling and Assimilation System (PIOMAS) reanalysis⁹. Between 2011
28 and 2020, Arctic sea ice thickness was 1.87 ± 0.10 m at the start of the melting season in May and 0.82 ± 0.11 m
29 by the end in August. Our year-round sea ice thickness record unlocks new opportunities for understanding Arctic
30 climate feedbacks on different timescales. For instance, sea ice volume observations from the early-summer may
31 extend the lead time of skilful August-October sea ice forecasts by several months, at the peak of the Arctic
32 shipping season.

33

34 **Main**

35 Sea ice thickness (SIT) is an essential climate variable that shapes almost every physical and biogeochemical
36 process operating at the Arctic air-ice-ocean interface. It guides human activities, as a platform for local Inuit
37 communities to travel³ and as a barrier and a key risk parameter for marine shipping¹⁰; it affects the amount of
38 sunlight reaching ice-associated or under-ice primary producers¹¹, which make up the base of the entire Arctic
39 food chain, particularly during summer months; and it helps to regulate the Arctic Ocean's biogeochemistry
40 including greenhouse gas fluxes¹². Regional SIT anomalies tend to have a longer 'memory' (~months) than sea
41 ice extent (SIE) anomalies (~days), dictating where thicker-than-usual sea ice can survive summer melting or
42 where thinner-than-usual sea ice melts away earlier in the season^{13,14}. Consequently, SIT observations –
43 particularly from the early summer⁷ – have the potential to extend operational sea ice forecasts by many months
44 ¹⁵.

45 Pan-Arctic maps of winter SIT have been produced from a satellite radar and laser altimetry record spanning 1993-
46 present^{16,17,18,19}, revealing that the sea ice cover has been rapidly thinning in response to climate warming²⁰.
47 However, meltwater ponds accumulating on Arctic sea ice between May and September have prevented
48 researchers from generating valid SIT observations in the summer months from any satellite sensor. This includes
49 the European Space Agency (ESA) radar altimeter CryoSat-2 which has collected observations all year round since
50 the mission was launched in 2010, but conventional algorithms have only enabled SIT to be derived for the winter
51 months of October to April¹⁸. Melt ponds complicate the interpretation of CryoSat-2 radar data, so it is difficult to
52 differentiate between sea ice and the open water leads that develop between sea ice floes²¹. Furthermore, melt
53 ponds bias the height measurement of the sea ice surface elevation above the water level (i.e., the ice freeboard)
54 which is critical for estimating its thickness⁸.

55 Summer SIT observations have been acquired on airborne campaigns and from in situ instruments such as moored
56 sonar that record the sea ice draft. These datasets have suggested that sea ice in the Arctic outflow region of Fram
57 Strait has thinned by up to 50% since 2000²² with a 25% decrease in the modal thickness of multi-year ice (MYI)
58 ²³ reflecting a strong decline in the age of sea ice surviving summer melt in the Arctic basin. However, airborne
59 and in situ observations give only limited snapshots of the ice thickness for a single day or location.

60 **Summer sea ice thickness from CryoSat-2**

61 In a recent study, deep learning was applied to CryoSat-2 radar returns to accurately distinguish sea ice floes from
62 leads, based on local variations in the radar echo response, for the months of May to September⁸. The sea ice radar
63 freeboard was then determined from the elevation difference between altimeter measurements of sea ice floes and
64 the sea level at leads. CryoSat-2 radar freeboard measurements capture the patterns and timing of summer sea ice
65 melting rates observed by independent airborne and in situ 'ground truth' sensors; however, they underestimate

66 the thickness of the thickest, roughest sea ice resident in the Central Arctic⁸. This is caused by an electromagnetic
67 (EM) range bias on the CryoSat-2 radar measurement associated with meltwater ponds lying at the sea ice surface.
68 Radar altimetry measurements of sea ice freeboard rely on accurate detection of the mean level of ice floe surfaces.
69 If the principal scattering horizon of the radar is not located at the same height as the mean ice floe surface height,
70 the altimeter range measurement will be biased. Arctic sea ice floe echoes are generally specular in the summer
71 months²¹ causing the waveform peak power to be referenced to the surface of reflecting ponds. Melt pond surfaces
72 typically lie below the mean elevation of the surrounding sea ice²⁴ causing a positive EM range bias over ice floes
73 which corresponds to an underestimation of the sea ice freeboard. This positive EM range bias is larger over
74 rougher sea ice⁸, equivalent to the well-understood sea state bias over open ocean where Ku-band radar altimeter
75 pulses are reflected more effectively by wave troughs than their crests²⁵.

76 Here we model the CryoSat-2 radar response over melt pond-covered sea ice and perform a set of simulations to
77 characterize the EM range bias (see Methods). The simulations confirm that radar range is increasingly
78 overestimated as the sea ice surface gets rougher, accounting for the observed underestimation of CryoSat-2
79 freeboard over rough sea ice in the Central Arctic⁸. We use auxiliary satellite estimates for the sea ice surface
80 roughness and melt pond coverage during Arctic summer months to obtain a quantitative prediction for the EM
81 range bias for every CryoSat-2 freeboard observation. The bias correction uncertainty is assessed through Monte
82 Carlo error analysis. Estimates of snow loading on the sea ice (from snow depth and density) using a Lagrangian
83 snow evolution scheme SnowModel-LG^{26,27} are then used to convert the CryoSat-2 summer radar freeboards to
84 SIT.

85 This approach enables us to create the first pan-Arctic all-year, decade long and gap free SIT record for 2011-2020
86 (available with the publication). By doing so, we take steps towards a goal of the future EU CRISTAL (Copernicus
87 Polar Ice and Snow Topography Altimeter) mission to provide “meaningful” SIT observations in summer²⁸. The
88 thickest pan-Arctic average SIT of 2.01 m was recorded in May 2015 whereas the thinnest SIT of 0.52 m was
89 recorded in October 2011. The interannual variability of SIT across our 2011-2020 record is smallest at 0.08 m in
90 the month of January and largest at 0.18 m in July. In Figure 1 we show for example biweekly (twice per month)
91 80-km resolution maps of SIT measured by CryoSat-2 over 2016. The record bridges two data processing
92 algorithms, for winter and summer months, but the spatial SIT distributions are generally consistent across the
93 transitions from April to May and from September to October. For instance, in 2016 sea ice was thinner than usual
94 in the Pacific sector of the Arctic, with a significant negative SIT anomaly appearing in February, growing to
95 around one meter by June (30% thinner than the 2011-2020 mean; Extended Data Fig. 6), and culminating in 7
96 weeks early ice edge retreat in the Beaufort Sea²⁹.

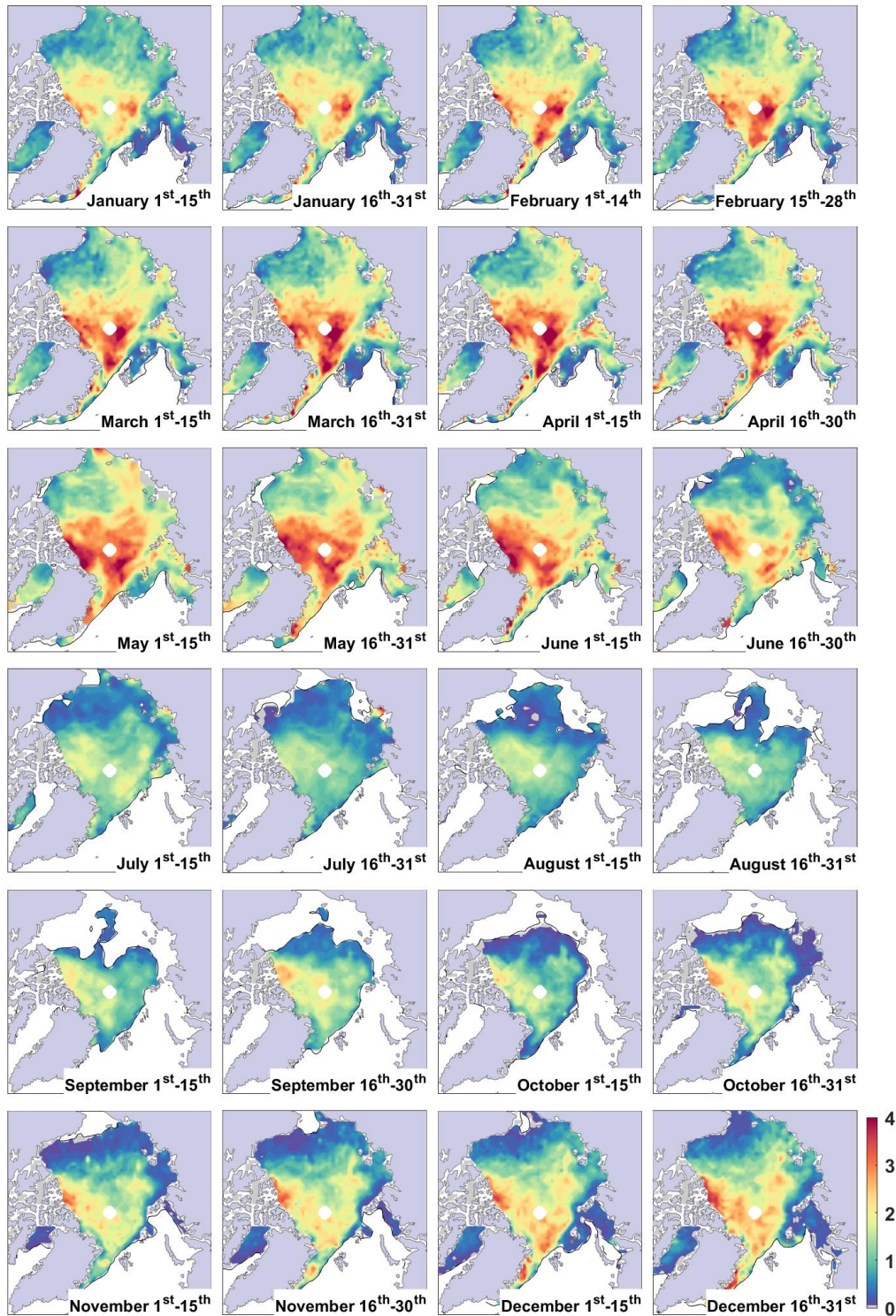


Figure 1 | Arctic sea ice thickness [m] measured over the entire year at biweekly (twice per month) intervals by CryoSat-2 in 2016. Observations for the cold season months of October-April are obtained from the LARM algorithm 44. Observations for the melting season months of May-September are obtained from the new method presented here (see Methods). Black contours represent the sea ice extent (15% ice concentration edge) and greyed-out areas represent missing data.

98 **Validating the ice thickness record**

99 We have validated the new satellite SIT observations against available airborne electromagnetic (AEM) sounding,
100 upward-looking sonar (ULS), and acoustic Doppler current profiler (ADCP) observations acquired over the Arctic
101 summer months. CryoSat-2 SIT can explain 80% of the variance (r^2) in coinciding helicopter-based AEM ice
102 thickness observations collected during the 2011 *TransArc* campaign of the Alfred Wegener Institute (AWI)
103 Polarstern Icebreaker, verifying the gradient of SIT from the Central Arctic to the sea ice edge recorded during
104 *TransArc* (Extended Data Fig. 2). The distribution of SIT north of Greenland recorded by AEM during AWI
105 *IceBird* campaigns from 2016-2018 is captured by CryoSat-2, although the satellite still underestimates the
106 thickness of the roughest sea ice³⁰ in coastal areas (Extended Data Fig. 3). This bias must be taken into account if
107 the observations are used, for instance, in future data assimilation experiments.

108 CryoSat-2 can likewise capture the timing and magnitude of ice melting rates recorded by ULS sensors on mooring
109 arrays at the Beaufort Gyre Exploration Program (BGEP) between 2011 and 2018 (Extended Data Fig. 4) and ULS
110 and ADCP sensors in the Laptev Sea between 2010 and 2015 (Extended Data Fig. 5). The satellite observations
111 can explain 71 and 54% of the variance (r^2) in the ice draft measured by BGEP and Laptev Sea arrays,
112 respectively. Furthermore, after removing the climatological mean seasonal cycles of ice draft from the three long
113 time series in the Beaufort Sea, the anomaly correlation coefficients between ULS and CryoSat-2 observations are
114 0.45, 0.51 and 0.37 for Moorings A, B and D, respectively. This suggests CryoSat-2 summer observations can
115 capture a significant portion of the interannual variability in sea ice thickness recorded by moored ULS sensors.

116 **Seasonal variability in sea ice volume**

117 Our new SIT observations allow us to quantify sea ice volume (SIV) throughout the melt season by integrating
118 CryoSat-2 sea ice thickness with ice concentration observations from OSISAF (see Methods). SIV anomalies are
119 then obtained from the time series of pan-Arctic total SIV, by removing the 2010-2020 climatological seasonal
120 cycle, and decomposed into the contributions from sea ice concentration and thickness anomalies (Extended Data
121 Fig. 7). This analysis demonstrates that SIT anomalies provide the dominant contribution to SIV interannual
122 variability, around five times higher than the absolute contribution from ice concentration anomalies. The
123 correlations between SIV anomalies and the anomalies of SIT, SIC and their correlated component, are 0.97, 0.27,
124 and 0.21, respectively.

125 We use the PIOMAS sea ice volume reanalysis system, which assimilates sea ice concentration and sea surface
126 temperature data³¹, as a benchmark for indirectly assessing our new observations. SIV derived from CryoSat-2
127 shows remarkable consistency with PIOMAS (Fig. 2a); the PIOMAS SIV is generally within the observation
128 uncertainty bounds, at the pan-Arctic scale and when separated into zones of predominantly first-year ice (FYI)
129 and multi-year ice (MYI). The strong correspondence between SIV time series from CryoSat-2 and PIOMAS are

130 supported by r^2 values and root-mean square errors of 0.95 (FYI: 0.96, MYI: 0.83) and 2350 km³ (FYI: 1190 km³,
 131 MYI: 1200 km³), respectively.

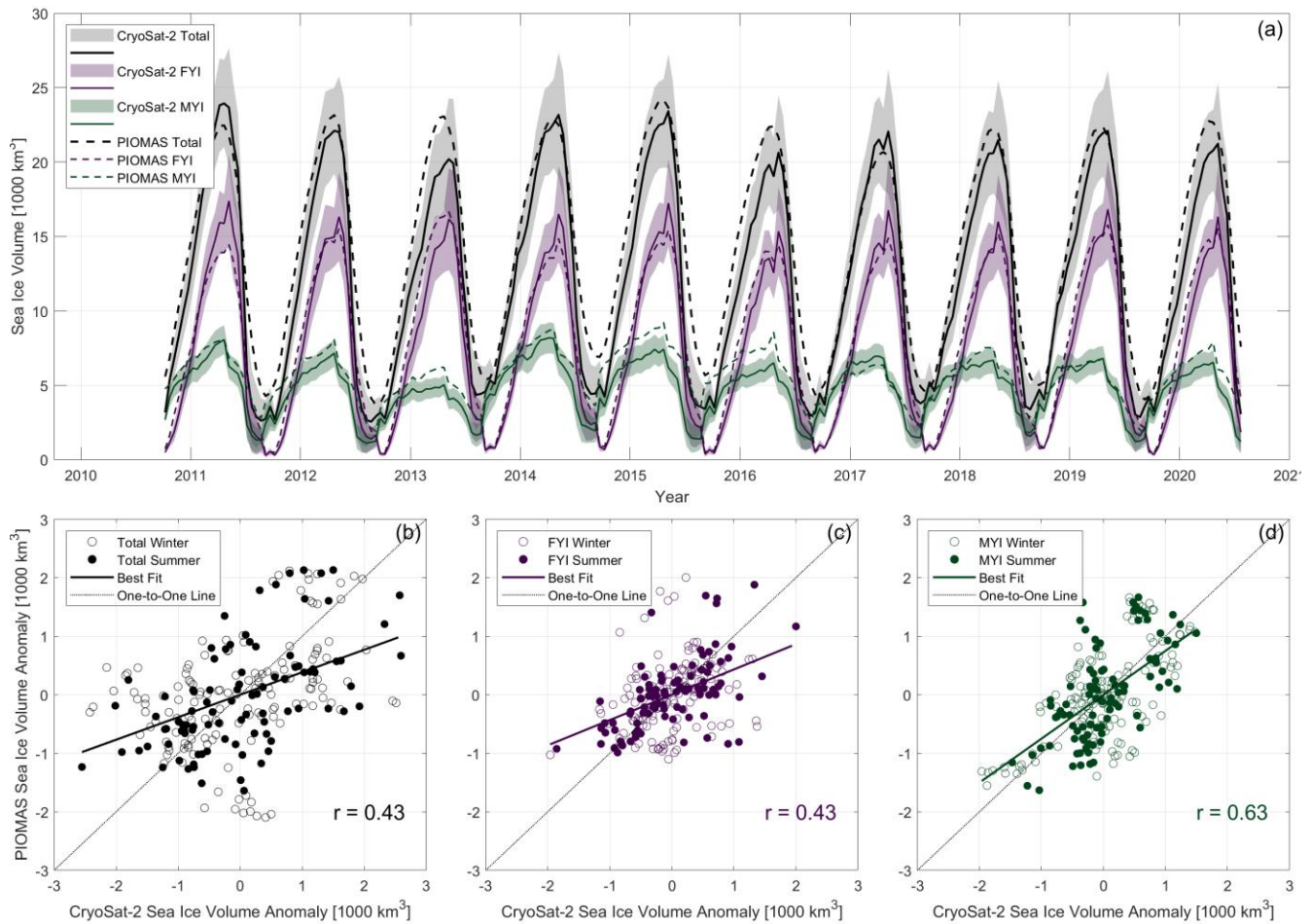


Figure 2 | Time series of sea ice volume derived from CryoSat-2 in comparison to reanalyzed predictions of ice volume from PIOMAS. (a) Sea ice volume from CryoSat-2 is presented with uncertainty envelopes for the entire Arctic and separated into zones of predominantly first-year ice and multi-year ice (using the NSIDC sea ice age dataset 46). The CryoSat-2 sea ice volume uncertainties are derived from the total ice thickness uncertainty (see Methods) multiplied by the ice area. (b)-(d) Scatterplots of the sea ice volume anomalies, for total, first-year and multi-year ice, respectively, after removing the climatological seasonal cycle of ice volume from the CryoSat-2 and PIOMAS time series.

132

133 SIV is typically higher from PIOMAS than CryoSat-2 around the September minimum. However, both the
 134 observations and reanalysis capture a reduction in MYI volume following the record Arctic SIE minimum in 2012
 135 and rebound in 2014 following reduced ice melt and strong ice convergence during summer 2013³². The anomaly
 136 correlation coefficients between PIOMAS and CryoSat-2 are 0.43 (FYI: 0.43, MYI: 0.63) after removing
 137 climatological mean seasonal cycles of SIV from both time series. Although CryoSat-2 SIT generally replicates

138 the seasonal cycle and magnitude of SIV from PIOMAS, the interannual variations in ice volume between datasets
139 are not identical and appear to agree better for MYI than for FYI (Fig. 2b-d). This could point to errors in the
140 satellite observations of SIT and/or limitations in the model-based reanalysis system.

141 **Covariance between ice volume and extent**

142 To further evaluate the new year-round satellite SIT record and verify that SIT anomalies persist through time
143 rather than being obscured by uncertainties (biases or random noise), we perform a lagged correlation analysis
144 between pan-Arctic SIV derived from CryoSat-2 and future pan-Arctic SIE from OSISAF (Fig. 3). Figure 3a
145 shows correlation coefficients between pan-Arctic total SIV and SIE, separated by a lag time between zero and
146 365 days, based on the full record of data between October 2010 and July 2020. (Note that sea ice within the
147 NSIDC *MASIE* Central Arctic region (Extended Data Fig. 9) is excluded from this analysis because the region has
148 been perennially ice covered over our study period). Time series for these correlations therefore correspond to 9-
149 11 years of CryoSat-2 data, depending on the target day, and generally do not exhibit statistically significant trends
150 over such short records. For robustness, we repeat the same analysis but detrend SIV and SIE time series before
151 calculating correlations (Extended Data Fig. 8); however, the major features of Figure 3 remain. We compare to a
152 reference analysis of lagged correlations between pan-Arctic total SIE and future SIE in Figure 3b.

153 Figure 3 illustrates statistically significant ($p < 0.1$) positive correlations between summer (June-September) SIE
154 and earlier ice volume/extent, starting from lead times between May and July. The lead times for significant
155 correlations increase over summer, matching the structure revealed by numerous idealized and operational model
156 sea ice prediction experiments^{7,13,14,33}. Our observational results therefore confirm the existence of a spring
157 predictability barrier, as suggested by previous modelling studies^{15,34}. Intense sea ice dynamics and new ice growth
158 in late winter can weaken the link between winter SIT anomalies and summer SIE²⁹, so that predictability is
159 subdued until melt onset¹⁵. Strong correlations between SIV and future SIE only develop when the sea ice-albedo
160 feedback acts to enhance existing SIT anomalies at the onset of the Arctic melt season³⁵.

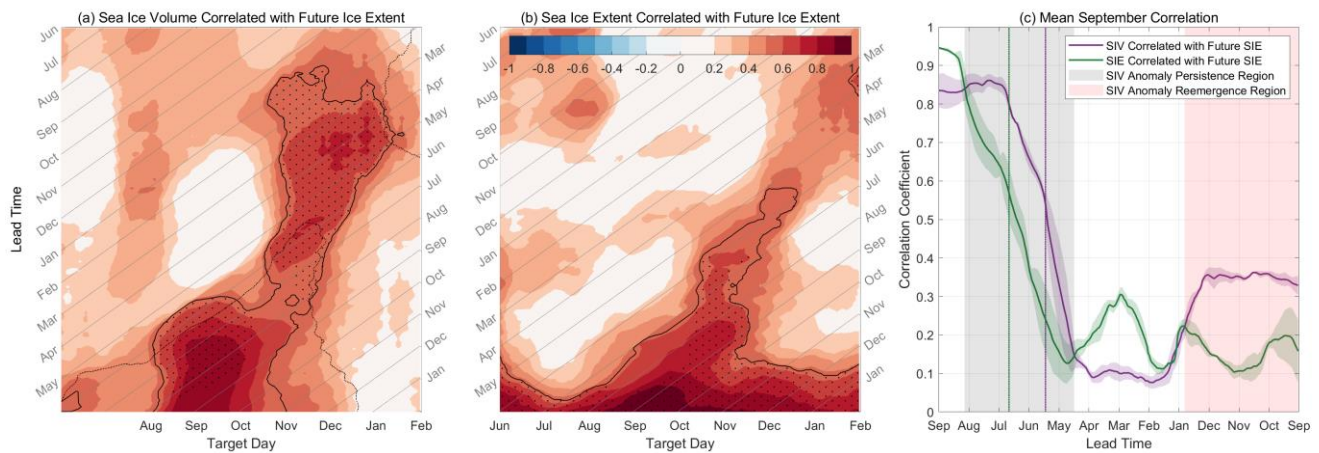


Figure 3 | Lag correlation plots between pan-Arctic sea ice volume and extent. (a) Correlations between SIV and later SIE and (b) correlations between SIE and later SIE. Black lines mark correlations with a statistical significance of $p = 0.1$ and stippling marks where SIV->SIE correlations are higher than SIE->SIE for (a) or vice versa for (b). The dotted line on (a) marks the correlations with a significance of $p = 0.1$ between PIOMAS SIV and later OSISAF SIE. The gray lines mark lead times for each month as contours. The lagged correlation can be identified on the plot where SIV/SIE at any lead month on the y axis intersects with future SIE for any target month on the x axis. (c) Mean (with standard deviation envelope) correlation for September SIE including two regions of predictability where SIV offers improvements over SIE. The two vertical lines mark the dates when correlations fall below $p = 0.1$. The same plot for detrended SIV and SIE time series is shown in Extended Data Figure 8.

161

162 **Future implications for forecasting**

163 For target months in the Arctic summer, SIE covaries strongly with future SIE at short lead times of around 0-45
 164 days (Fig. 3b), whereas SIV takes over as the dominant source of skill for predicting ice extent between August
 165 and December over leads of 45-300 days (Fig. 3a). For instance, SIV is the dominant source of skill for predicting
 166 September SIE at lead times of 25-140 days (Fig. 3c) which is generally consistent with operational sea ice
 167 forecasting systems¹³. SIT anomalies in our year-round CryoSat-2 dataset must be larger than the observation
 168 uncertainties, because strong correlations between SIV and SIE bridge the transitions between conventional winter
 169 and new summer processing algorithms. Since there are significant ($p < 0.1$) correlations between SIE in September
 170 and SIV over 3.5 months earlier, in mid-May, compared to only 2 months earlier in late-June for SIE (Fig. 3c),
 171 new summer SIT observations may also be valuable in future to extend the lead time of Arctic sea ice forecasts.

172 Our results further reveal the reemergence of SIV as a potential source of skilful ice extent predictability in autumn
 173 months (Fig. 3a). The lead times for this reemergence region are between 100-310 days, suggesting that October-
 174 December SIE can be accurately forecast from SIV measured by CryoSat-2 as early as the preceding January-

175 February, but not after July-August. Correlations between SIV and SIE are more uncertain for this reemergence
176 region (Extended Data Fig. 10) and weaker – but still present – when time series are detrended (Extended Data
177 Fig. 8). The skill is mainly sourced from the Beaufort, Chukchi, and East Siberian Seas where the sea ice can be
178 less dynamic than in other regions (Extended Data Fig. 9). These results offer the exciting potential for SIT
179 observations enhancing future sea ice forecasts that bridge the spring and summer. For instance, CryoSat-2 SIV
180 extends the lead time for skilful ice extent predictability in autumn by several months compared to using PIOMAS
181 reanalysed SIV (Fig. 3a).

182 Autumn SIE predictions at leads up to around 200 days (Fig. 3a) can be explained by the persistence of early melt
183 season SIT anomalies, whereas the correlations at leads <100 days are obscured by new ice formation in October
184 and November. However, the skilful SIE forecasts at leads up to 280-310 days can only be explained by
185 reemergence of winter SIT anomalies in the following autumn. This could potentially occur via sequential hand-
186 off from winter SIT anomalies to spring SIE anomalies to summer upper ocean heat anomalies to autumn SIE
187 anomalies^{34,36}. So-called ‘growth-to-melt’ season reemergence represents the exchange of anomalies between sea
188 ice area and thickness¹³. The two properties covary during the summer but not in winter³⁶, with positive regional
189 winter SIT anomalies slowing down sea ice retreat in the following spring and creating positive summer SIE
190 anomalies, or vice versa³⁷. A shorter open water season limits solar heating of the upper ocean, which extends this
191 predictability regime via the ‘melt-to-growth’ reemergence mechanism³⁶. Our observational results reinforce
192 modelling studies that find SIV is a better predictor than SIE for July-November ice extent 6-10 months in advance
193¹³.

194 **Next steps**

195 The pan-Arctic summer SIT product presented here could benefit from a number of improvements. Dedicated
196 airborne campaigns to simultaneously measure the Ku-band radar response, surface roughness, freeboard and
197 thickness of melt pond-covered sea ice are required to better understand the EM radar range bias. The evolutions
198 of FYI and MYI densities with summer brine drainage and meltwater flushing are poorly understood³⁸. Gap-free
199 and consistent satellite data products for Arctic summer melt pond fraction and surface roughness are needed to
200 improve the application of freeboard bias corrections. Finally, a greater emphasis on collecting SIT validation
201 datasets during the Arctic summer – especially in the shoulder months of May and September – is essential for
202 evaluating new satellite products.

203 Future near-real time summer altimetry SIT observations could improve the safety of Arctic shipping through
204 integration into the Polar Operational Limit Assessment Risk Index System (POLARIS)³⁹ that has been developed
205 under the International Maritime Organization’s (IMO) Polar Code. Quantifying sea ice thickness, compared to
206 qualitatively characterizing “ice conditions” within the code, offers the critical information required to guide
207 go/no-go decisions for Arctic vessels⁵ and make future projections of Arctic navigation risks¹⁰. ‘Missing’ summer
208 SIT observations have also impacted many fields of Arctic research beyond seasonal sea ice forecasting. For

209 instance, SIT is needed to close the energy budget of the Arctic Ocean during summer months ⁴⁰; to determine
210 pelagic and sympagic primary productivity during the active summer bloom ⁴¹; to reconcile the greenhouse-gas
211 balance of the Arctic ⁴²; and to validate and improve the representation of sea ice in global coupled climate models
212 ⁴¹. Our freely-available summer SIT dataset opens new research opportunities in all areas of Arctic system science.

213

1. Notz, D. & Stroeve, J., Observed Arctic sea-ice loss directly follows anthropogenic CO₂ emission. *Science* **354** (6313), 747-750 (2016).
2. Kinnard, C. *et al.*, Reconstructed changes in Arctic sea ice over the past 1,450 years. *Nature* **479** (7374), 509-512 (2011).
3. Eicken, H., Arctic sea ice needs better forecasts. *Nature* **497** (7450), 431-433 (2013).
4. Kwok, R., Spreen, G. & Pang, S., Arctic sea ice circulation and drift speed: Decadal trends and ocean currents. *J. Geophys. Res. Oceans* **118** (5), 2408-2425 (2013).
5. Mudryk, L. R. *et al.*, Impact of 1, 2 and 4 °C of global warming on ship navigation in the Canadian Arctic. *Nat. Clim. Ch.* **11** (8), 673-679 (2021).
6. Kern, S. *et al.*, Satellite passive microwave sea-ice concentration data set intercomparison: closed ice and ship-based observations. *Cryosphere* **13**, 3261-3307 (2019).
7. Bushuk, M. *et al.*, Skillful regional prediction of Arctic sea ice on seasonal timescales. *Geophys. Res. Lett.* **44** (10), 4953-4964 (2017).
8. Dawson, G. *et al.*, A 10-year record of Arctic summer sea ice freeboard from CryoSat-2. *Rem. Sens. Env.* **268**, 112744 (2022).
9. Zhang, J. & Rothrock, D. A., Modeling Global Sea Ice with a Thickness and Enthalpy Distribution Model in Generalized Curvilinear Coordinates. *Mon. Wea. Rev.* **131**, 845–861 (2003).
10. Aksenov, Y. *et al.*, On the future navigability of Arctic sea routes: High-resolution projections of the Arctic Ocean and sea ice. *Marine Pol.* **75**, 300-317 (2017).
11. Stroeve, J. C. *et al.*, A multi-sensor and modelling approach for mapping light under sea ice. *Front. Mar. Sci.* (2021).
12. Parmentier, F. J. W. *et al.*, The impact of lower sea-ice extent on Arctic greenhouse-gas exchange. *Nature Clim. Ch.* **3** (3), 195-202 (2013).
13. Guemas, V. *et al.*, A review on Arctic sea-ice predictability and prediction on seasonal to decadal time-scales. *Quat. J. Royal Met. Soc.* **142** (695), 546-561 (2016).
14. Ordoñez, A. C., Bitz, C. M. & Blanchard-Wrigglesworth, E., Processes controlling Arctic and Antarctic sea ice predictability in the Community Earth System Model. *J. Clim.* **31** (23), 9771-9786 (2018).
15. Bushuk, M., Winton, M., Bonan, D. B., Blanchard-Wrigglesworth, E. & Delworth, T., A mechanism for the Arctic sea ice spring predictability barrier. *Geophys. Res. Lett.* **47** (13) (2020).
16. Laxon, S., Peacock, N. & Smith, D., High interannual variability of sea ice thickness in the Arctic region. *Nature* **425** (6961), 947-950 (2003).
17. Kwok, R. & Cunningham, G. F., ICESat over Arctic sea ice: Estimation of snow depth and ice thickness. *J. Geophys. Res.* **113**, C08010 (2008).
18. Laxon, S. W. *et al.*, CryoSat-2 estimates of Arctic sea ice thickness and volume. *Geophys. Res. Lett.* **40**, 732-737 (2013).
19. Petty, A. A., Kurtz, N. T., Kwok, R., Markus, T. & Neumann, T. A., Winter Arctic Sea Ice Thickness From ICESat-2 Freeboards. *J. Geophys. Res. Oceans* **125** (5), e2019JC015764 (2020).
20. Kwok, R., Arctic sea ice thickness, volume, and multiyear ice coverage: losses and coupled variability (1958–2018). *Env. Res. Lett.* **13** (10), 105005 (2018).
21. Kwok, R., Cunningham, G. F. & Armitage, T. W. K., Relationship between specular returns in CryoSat-2 data, surface albedo, and Arctic summer minimum ice extent. *Elem. Sci. Anth.* **6** (1), 53 (2018).
22. Renner, A. H. *et al.*, Evidence of Arctic sea ice thinning from direct observations. *Geophys. Res. Lett.* **41** (14), 5029-5036 (2014).
23. Belter, H. J. *et al.*, Interannual variability in Transpolar Drift summer sea ice thickness and potential impact of Atlantification. *Cryosphere* **15** (6), 2575-2591 (2021).

24. Eicken, H., Grenfell, T. C., Perovich, D. K., Richter-Menge, J. A. & Frey, K., Hydraulic controls of summer Arctic pack ice albedo. *J. Geophys. Res.* **109**, C08007 (2004).
25. Melville, W. K. *et al.*, Measurements of electromagnetic bias in radar altimetry. *J. Geophys. Res. Oceans* **96** (C3), 4915-4924 (1991).
26. Liston, G. E. *et al.*, A Lagrangian snow-evolution system for sea-ice applications (SnowModel-LG): Part I—Model description. *J. Geophys. Res. Oceans* **125** (10) (2020).
27. Stroeve, J. *et al.*, A Lagrangian snow evolution system for sea ice applications (SnowModel-LG): Part II—Analyses. *J. Geophys. Res. Oceans* **125** (10), e2019JC015900 (2020).
28. Kern, M. *et al.*, The Copernicus Polar Ice and Snow Topography Altimeter (CRISTAL) high-priority candidate mission. *Cryosphere* **14** (7), 2235-2251 (2020).
29. Babb, D. G., Landy, J. C., Barber, D. G. & Galley, R. J., Winter sea ice export from the Beaufort Sea as a preconditioning mechanism for enhanced summer melt: A case study of 2016. *J. Geophys. Res.* **124** (9), 6575-6600 (2019).
30. Farrell, S. L., Duncan, K., Buckley, E. M., Richter-Menge, J. & Li, R., Mapping sea ice surface topography in high fidelity with ICESat-2. *Geophys. Res. Lett.* **47** (21), e2020GL090708 (2020).
31. Schweiger, A. *et al.*, Uncertainty in modeled Arctic sea ice volume. *J. Geophys. Res.* **116**, C00D06 (2011).
32. Kwok, R., Sea ice convergence along the Arctic coasts of Greenland and the Canadian Arctic Archipelago: Variability and extremes (1992–2014). *Geophys. Res. Lett.* **42** (18), 7598-7605 (2015).
33. Bonan, D. B., Bushuk, M. & Winton, M., A spring barrier for regional predictions of summer Arctic sea ice. *Geophys. Res. Lett.* **46** (11), 5937-5947 (2019).
34. Day, J. J., Hawkins, E. & Tietsche, S., Will Arctic sea ice thickness initialization improve seasonal forecast skill? *Geophys. Res. Lett.* **41** (21), 7566-7575 (2014).
35. Schröder, D., Feltham, D. L., Flocco, D. & Tsamados, M., September Arctic sea-ice minimum predicted by spring melt-pond fraction. *Nature Clim. Change* **4**, 353-357 (2014).
36. Blanchard-Wrigglesworth, E., Armour, K. C., Bitz, C. M. & DeWeaver, E., Persistence and inherent predictability of Arctic sea ice in a GCM ensemble and observations. *J. Clim.* **24** (1), 231-250 (2011).
37. Chevallier, M. & Salas-Méllia, D., The role of sea ice thickness distribution in the Arctic sea ice potential predictability: A diagnostic approach with a coupled GCM. *J. Clim.* **25** (8), 3025-3038 (2012).
38. Eicken, H. *et al.*, Thickness, structure, and properties of level summer multiyear ice in the Eurasian sector of the Arctic Ocean. *J. Geophys. Res. Oceans* **100** (C11), 22697-22710 (1995).
39. Stoddard, M. A., Etienne, L., Fournier, M., Pelot, R. & Beveridge, L., *Making sense of arctic maritime traffic using the polar operational limits assessment risk indexing system (POLARIS)*, presented at IOP Conference series: Earth and environmental science, 2016 (unpublished).
40. Perovich, D., Light, B. & Dickinson, S., Changing ice and changing light: trends in solar heat input to the upper Arctic ocean from 1988 to 2014. *Ann. Glaciol.* **61** (83), 401-407 (2020).
41. Schröder, D., Feltham, D. L., Tsamados, M., Ridout, A. & Tilling, R., New insight from CryoSat-2 sea ice thickness for sea ice modelling. *Cryosphere* **13**, 125-139 (2019).

216 **Methods**

217 **CryoSat-2 sea ice radar freeboards**

218 Sea ice thickness observations are derived from the ESA CryoSat-2 radar altimeter⁴⁴ following the processing
219 chain illustrated in Extended Data Figure 1. The first step of this method, documenting a new record of sea ice
220 radar freeboard measurements obtained from CryoSat-2 over the Arctic summer ‘melt season’ months of May-
221 September, 2011-2020, has already been published⁸. The algorithm to obtain radar freeboard involved several
222 steps. (1) Fitting the SAMOSA+ (SAR Altimetry MOde Studies and Applications +) analytical radar echo model
223⁴⁵ to observed waveforms to retrack the ice or ocean surface elevation. Model fitting was performed using the ESA
224 Grid Processing On Demand (GPOD) *SARvatore* and *SARInvatore* services. (2) Classification of radar waveforms
225 into returns from sea ice floes and leads using a 1D convolutional neural network (CNN). The CNN was trained
226 using CryoSat-2 samples selected over known surface types (sea ice floes or leads) identified in coincident satellite
227 optical and SAR imagery, as described in Dawson et al.⁸. (3) Finding the height difference between ice floe
228 elevations and sea level. (4) Sampling the CryoSat-2 along-track radar freeboards to biweekly, 80 km resolution
229 grids through inverse distance- and time-weighted linear interpolation.

230 Hereafter, the methods section describes new techniques, building on Dawson et al.⁸, to (1) characterize and
231 correct for the EM range bias on CryoSat-2 radar freeboard observations, (2) convert freeboards to estimates of
232 sea ice thickness with associated uncertainties, (3) reconcile summer and winter SIT records, (4) validate new SIT
233 observations, and (5) perform lagged correlation analyses between SIE and SIV.

234 **Characterization of the EM range bias**

235 Ideally, we would correct for the EM range bias over melt pond-covered sea ice floes at the radar waveform
236 retracking step. However it would be extremely challenging – potentially impossible – to invert for the EM range
237 bias correction solely from the shape of a CryoSat-2 waveform. Consequently, we estimate the EM bias separately
238 then apply it as a correction to the biweekly 80-km radar freeboard product derived in Dawson et al.⁸. The radar
239 range bias is quantified by comparing a set of numerical waveform simulations from sea ice surfaces with the
240 Facet-Based Echo Model (FBEM)^{46,42}, that integrates melt ponds, to solutions from the SAMOSA+ analytical echo
241 model used for waveform retracking. Full details of the rationale for this approach, the waveform simulations, and
242 the bias quantification are given in Supplementary Information Section A and references^{47,48,49,50,51,52}.

243 We simulate the backscattered CryoSat-2 radar response with FBEM from random sea ice surfaces generated with
244 a prescribed roughness height standard deviation σ and randomly distributed melt pond coverage f_p . Melt ponds
245 are distributed by accumulating water on the topography below a threshold elevation until the coverage equals f_p ,
246 with all pond surfaces sitting at the same elevation. Relevant parameters for modelling the sea ice surface
247 backscattering coefficients are obtained from the literature, including ‘radar scale’ (mm-cm) melt pond surface
248 roughness parameters based on field observations of melt pond wave spectra⁵³. Melt pond surface roughness varies

249 as a function of the wind speed U_{10} , so we run simulations with FBEM covering a wind speed range from 5-7 ms⁻¹
250 to characterize the uncertainty of this parameter. A lookup table (LUT) of altimeter echoes is generated from the
251 average of 100 model outputs for each combination of σ from 0 to 60 cm in 2 cm intervals and f_p from 0 to 0.6 in
252 0.02 intervals. Since each model run is based on a randomly-generated surface, we have to average 100 model
253 outputs to accurately characterize the echo for a certain combination of σ and f_p .

254 The numerical FBEM simulations from pond-covered sea ice are assumed to represent ‘true’ radar echoes for
255 certain combinations of σ and f_p , and then used as a reference for evaluating the SAMOSA+ retracking algorithm
256 applied in our CryoSat-2 radar freeboard processing scheme⁸. We find the best fit SAMOSA+ model solution for
257 each FBEM echo in the LUT, with the EM range bias then defined as the two-way travel time difference between
258 echo retracking points. This produces a theoretical quantitative estimate for the EM range bias as a two-
259 dimensional function of σ and f_p which can then be applied as a correction on the CryoSat-2 derived radar
260 freeboard.

261 Auxiliary estimates for the sea ice surface roughness and melt pond coverage during Arctic summer months are
262 required to apply the theoretical range bias correction. At the time of writing, there is no consistent pan-Arctic
263 gap-free dataset available for either parameter covering the study period from 2011-2020. We obtain pan-Arctic
264 sea ice surface roughness observations for summer months by propagating CryoSat-2 estimates of σ from the 25-
265 km gridded Lognormal Altimeter Retracker Model (LARM) dataset⁴² forward and backward from winter months,
266 based on observations of the sea ice drift. These roughness observations are assumed to represent the standard
267 deviation of the snow-sea ice interface. Daily observations of sea ice drift are obtained from the NSIDC Polar
268 Pathfinder dataset <https://nsidc.org/data/nsidc-0116/versions/4>⁴³. A single estimate of σ is derived for each
269 biweekly 80-km CryoSat-2 freeboard grid, between May and September, by sampling the inverse-time weighted
270 average of evolved Lagrangian April and October σ fields at each grid point. We estimate uncertainty on the
271 roughness from the root sum square of the measurement uncertainty and the absolute difference between forward
272 and backward predictions.

273 Remotely sensed observations of melt pond fraction are obtained from the Sentinel-3 OLCI sensor through the
274 University of Bremen <https://seaice.uni-bremen.de/melt-ponds/>. This is a daily 12.5 km pan-Arctic product based
275 on the Version 1.5 algorithm of Istomina et al.⁵⁴ and covering the period between 2017 and 2020. Since cloud
276 cover can heavily obscure the coverage of daily observations and only the final four years of our freeboard record
277 had coinciding measurements of f_p , we calculate a seasonal climatology of the f_p observations that we could then
278 apply to all years of our study 2011-2020. Biweekly 80-km melt pond fraction fields are obtained from the average
279 of all cloud-free OLCI pixels between 2017 and 2020 within each two-week summer window and 80-km grid cell.
280 The f_p climatology captures the expected seasonal cycle of melt pond formation, growth, and drainage²⁴, and
281 regional patterns in coverage reflecting the pan-Arctic differences between sea ice types⁵⁵. However, it does not
282 account for interannual variations in f_p within the same region, which can be significant⁵⁶, and represent an

283 uncertainty on our observations. We estimate the uncertainty on our melt pond climatology from the root sum
284 square of the f_p pixel standard deviation and the interannual variability of f_p between years of the 2017-2020
285 record.

286 The EM range bias correction Δh_r is calculated from inputs of σ from CryoSat-2 and f_p from Sentinel-3 OLCI,
287 and then added to the CryoSat-2 radar freeboard estimates. This correction is not applicable when a significant
288 snowpack is present on the sea ice surface, so that melt pond coverage would be limited. Therefore, we do not
289 apply the correction when snow depth (see below) $h_s > 60$ cm and reduce the correction linearly as a function of
290 snow depth between 0 and 60 cm (i.e., $\Delta h_r * (1 - h_s/60)$).

291 Uncertainty on the bias correction is assessed through Monte Carlo error analysis. For each value of the EM range
292 bias, we have estimates for the uncertainties of three input parameters: σ , f_p , and the radar-scale melt pond
293 roughness induced by variable wind speed U_{10} . We recalculate the bias 1000 times but each time including
294 randomly selected errors from the error distributions of σ , f_p and U_{10} , obtaining the total uncertainty from the
295 standard deviation of these 1000 iterations. We assume that σ and f_p have Gaussian distributed errors with standard
296 deviations equal to the parameter uncertainties, but that radar-scale melt pond roughness values are equally likely
297 over the modelled range of U_{10} between 5 and 7 ms^{-1} . The final uncertainty of the bias-corrected CryoSat-2 radar
298 freeboard is obtained from the root sum square of the uncertainty on the EM bias correction and the measured
299 freeboard variability within each 80-km grid cell. The uncertainty is highest (up to around 40% of the corrected
300 freeboard) between July and August when the EM range bias correction is largest.

301 **Sea ice thickness and uncertainty**

302 Snow load (depth and density) estimates are obtained from the Lagrangian snow evolution scheme SnowModel-
303 LG ^{26,27}. This scheme uses the MERRA2 atmospheric reanalysis and NSIDC Polar Pathfinder ice motion
304 observations to simulate the accumulation of snow on Arctic sea ice between September and April, while also
305 modelling snowpack metamorphism and melt between May and August. Snow carryover between accumulation
306 seasons is minimal and the snow melting season is around 6 weeks in length ²⁶. Snow melt occurs between May
307 and July but is most rapid in June reflecting the transition from a negative to positive Arctic surface energy balance,
308 before the snow accumulates again slowly from September. SnowModel-LG can reproduce the timing of snowmelt
309 from in situ observations but has difficulty predicting rates of melt ²⁷. We assume relatively high constant
310 uncertainties in snow depth and density of 10 cm and 50 kg m^{-3} , respectively, (or 50% if the depth or density are
311 below these values). These uncertainties are based on the comparisons between SnowModel-LG data and those
312 from independent datasets, including Operation IceBridge, ice mass balance buoys, snow buoys and MagnaProbes
313 ²⁷.

314 CryoSat-2 radar freeboards show clear unrealistic thickening between April and May ⁸ resulting from the radar
315 signal attenuating within the melting snowpack ⁵⁷ rather than penetrating to the snow-ice interface. This is likely

316 resulting from increasing moisture content within the snowpack causing scattering and absorption of the CryoSat-
 317 2 Ku-band EM wave. The depth of radar penetration into the snow will vary between regions, years and potentially
 318 from observation-to-observation along the satellite track, depending on the snow geophysical properties
 319 (roughness, microstructure, density, volume salinity) and atmospheric conditions (temperature, moisture content,
 320 etc.)^{57,58,59,60}. Since we cannot predict these variations in the penetration depth, as a first approximation we assume
 321 the Ku-band radar penetrates a constant 90% of the snow cover wherever snow is present between May and
 322 September, which produces a largely consistent transition derived sea ice thickness between April and May, and
 323 between September and October. However, the assumed Ku-band radar penetration depth into snow during the
 324 Arctic melting season does impact the estimated sea ice thickness (see Supplementary Information Section B) and
 325 should therefore be the subject of further study.

326 Sea ice thickness h_i is obtained from the hydrostatic equation, accounting for snow loading above the radar
 327 penetration depth fraction δ_p and for the different densities of snow and sea ice below it as follows

$$h_i = \frac{h_s \rho_w - h_f \rho_w - h_s \rho_s - \delta_p h_s \rho_w}{\rho_i - \rho_w} \quad (1)$$

328 Where h_f is the sea ice freeboard, ρ_w , ρ_s , and ρ_i are the densities of ocean water, snow, and sea ice, and h_s is the
 329 snow depth. δ_p is the mean radar penetration expressed as a fraction of the snow depth, which here we assume is
 330 equal to 0.9. We apply the following function adapted from Mallett et al.⁶¹ to correct for delayed radar wave
 331 propagation through the snowpack and convert from bias-corrected measured radar freeboard h_{rf} to bias-corrected
 332 sea ice freeboard

$$h_f = h_{rf} + \delta_p h_s ((1 + 0.51 \rho_s / 1000)^{1.5} - 1) \quad (2)$$

333 (Note that we use the term ‘measured’ radar freeboard because we are not assuming that the measured radar
 334 freeboard coincides with the actual radar freeboard of the snow-ice interface).

335 The ocean water density ρ_w is assumed to be 1024 kg m⁻³. The sea ice density is assumed to be 917 and 882 kg m⁻³
 336 ³ for FYI and MYI, respectively, following Alexandrov et al.⁶². We use the NSIDC weekly 12.5 km sea ice age
 337 product V4 <https://nsidc.org/data/nsidc-0611> to differentiate between zones of FYI and MYI. Constant sea ice
 338 type-dependent densities are used here to maintain consistency with CryoSat-2 sea ice thickness processing in cold
 339 season months⁶³; however, we can expect ice densities to vary significantly over the course of the summer melting
 340 season³⁸ and between regions⁶². Uncertainty on the sea ice density is assumed to be 35.7 kg m⁻³ for FYI and 23.0
 341 kg m⁻³ for MYI, multiplied by $1/\sqrt{N}$ with N the number of individual CryoSat-2 freeboard observations in an 80-
 342 km grid cell, following previous studies⁶³. Snow depths and densities are from SnowModel-LG.

343 An example for the annual Arctic Ocean sea ice thickness evolution in 2016 is shown in Figure 1 within the main
 344 paper, incorporating cold-season observations from the LARM (Lognormal Altimeter Retracker Model) algorithm
 345 ⁴² and melt-season observations from our new method described here. The sea ice thickness data for winter months

346 (October-April) are an updated ESA Baseline-D version of the Baseline-C dataset available here
 347 <https://data.bas.ac.uk/full-record.php?id=GB/NERC/BAS/PDC/01257>. The LARM algorithm accounts for
 348 variable sea ice surface roughness and backscattering properties⁴⁶, to derive radar freeboard for Arctic winter
 349 months⁴². We discuss the consistency between winter and summer SIT records below.

350 Uncertainty on the sea ice thickness is estimated from the individual uncertainties ε on four parameters: h_f , h_s ,
 351 ρ_s , ρ_i , at the 80 km grid scale of the thickness observations. Assuming uncertainties between these variables are
 352 uncorrelated at 80 km scale, the total random thickness error ε_{h_i} is determined by Gaussian propagation of
 353 uncertainty as:

$$\varepsilon_{h_i}^2 = \left(\frac{\partial h_i}{\partial h_f} \varepsilon_{h_f} \right)^2 + \left(\frac{\partial h_i}{\partial h_s} \varepsilon_{h_s} \right)^2 + \left(\frac{\partial h_i}{\partial \rho_s} \varepsilon_{\rho_s} \right)^2 + \left(\frac{\partial h_i}{\partial \rho_i} \varepsilon_{\rho_i} \right)^2 \quad (3)$$

354 Where the partial derivatives of Eq. 3 are used as weights for the variances of individual parameters to obtain their
 355 contribution to the ice thickness uncertainty:

$$\frac{\partial h_i}{\partial h_f} = \frac{\rho_w}{\rho_w - \rho_i}$$

$$\frac{\partial h_i}{\partial h_s} = \frac{\rho_w - \rho_s - \delta_p \rho_w}{\rho_i - \rho_w}$$

$$\frac{\partial h_i}{\partial \rho_s} = \frac{h_s}{\rho_w - \rho_i}$$

$$\frac{\partial h_i}{\partial \rho_i} = \frac{h_f \rho_w + h_s \rho_s - h_s \rho_w + \delta_p h_s \rho_w}{(\rho_w - \rho_i)^2}$$

(4)

356 Median ice thickness uncertainty for summer months is estimated to be 33% of the thickness for FYI and 40% for
 357 MYI. Of this, the freeboard uncertainty dominates, contributing 80-90% of the total thickness uncertainty, with
 358 the snow depth then sea ice density uncertainties contributing most of the remaining 10-20%.

359 **Reconciling summer and winter CryoSat-2 sea ice thickness records**

360 The algorithms for generating sea ice thickness observations from CryoSat-2 vary between summer (May-
 361 September) and winter (October-April) conditions. We use many of the same steps in both processing algorithms,
 362 including the same SnowModel-LG snow depth and density product, the same constant sea ice densities for FYI
 363 and MYI, and the same method for uncertainty propagation; however, other steps are necessarily different. To
 364 evaluate the consistency between these datasets, we examine the transitions in ice thickness and thickness
 365 anomalies across the ‘shoulder’ months of April-May and September-October. Figure 2 in the main paper
 366 illustrates that sea ice volume from CryoSat-2 typically varies smoothly across the shoulder months. Only in a few

367 years (2014 at Mooring B and 2017 at Mooring D) does the CryoSat-2 time series of sea ice draft appear to jump
368 between April and May in the Beaufort Sea (Extended Data Fig. 4). The patterns of sea ice thickness shown in
369 Figure 1 of the main paper do not change appreciably across the shoulder months, with the exception of new thin
370 sea ice in the MIZ at the end of September which appears to be overestimated compared to the same locations in
371 early October. Thin ice retrieval is a known limitation of the summer radar freeboard algorithm ⁸.

372 Importantly, sea ice thickness anomalies persist from winter to summer and back to winter months at the same
373 locations, which we would not expect to see if uncertainty exceeded the CryoSat-2 ice thickness signal. For
374 instance, a negative sea ice thickness anomaly appears in the Pacific Sector of the Arctic in February 2016, grows
375 to >1 m (~30% thinner than the 2011-2020 average) by May-June, before sea ice in the Beaufort Sea broke up and
376 melted away completely 7 weeks earlier than usual in August (Extended Data Fig. 6). Babb et al. ²⁹ showed that
377 anomalously high sea ice export and divergence promoted the formation of thin ice between February and April
378 that preconditioned sea ice in the Beaufort Sea for early break up and only the second ice-free Beaufort Sea on
379 record. This a perfect example of the regional ‘growth-to-melt season reemergence’ discussed in the main paper
380 and now measurable by our summer CryoSat-2 thickness product. By contrast, a positive SIT anomaly appears in
381 the Kara Sea in June (Extended Data Fig. 6) and persists through summer into the following sea ice growth season,
382 leading to >1 m thicker sea ice than usual in this region by the end of 2016.

383 **Validation against independent datasets**

384 Gridded CryoSat-2 sea ice thickness observations are validated against independent measurements of sea ice
385 thickness from airborne EM (AEM) induction datasets ^{23,64} from the Central Arctic Ocean and Lincoln Sea, and sea
386 ice draft from mooring ULS arrays in the Beaufort and Laptev Seas, and in Fram Strait. All validations are
387 presented for the first time here.

388 *Airborne EM Data*

389 The AEM dataset includes observations from the AWI Polarstern ARK-XXVI/3 *TransArc* campaign in 2011 ⁶⁴,
390 available from <https://doi.org/10.1594/PANGAEA.937197>, and the *IceBird* campaigns from 2016 to 2018 ²³. For
391 the *TransArc* campaign the sensor was attached to a helicopter and collected ice thickness observations over small
392 surveys around the Polarstern research vessel in the Central Arctic Ocean (Extended Data Fig. 2) between August
393 and September. In the *IceBird* campaigns the sensor was towed by a fixed-wing aircraft and collected ice thickness
394 observations over large surveys covering the coast of Northern Greenland and the Fram Strait in late-July and
395 August (Extended Data Fig. 3). The AEM sensor estimates sea ice thickness by measuring the electrical
396 conductivity difference between ice and ocean water and is estimated to have an uncertainty of ± 0.1 m over level
397 ice ⁶⁵ but accuracy can be reduced in the presence of melt ponds ⁶⁶. The airborne observations have a footprint on
398 the scale of 10s of meters, so we average them to 80 kilometers before comparing to CryoSat-2.

399 The CryoSat-2 observations in August-September 2011 match very closely to the AEM data acquired on TransArc.
400 They can explain 80% of the variance in the AEM data, with a mean difference of -16 cm (CryoSat-2 minus AEM)
401 and an RMSE of only 13 cm (Extended Data Fig. 2). Satellite data mostly capture the range in average thickness
402 between the Central Arctic MYI pack ice in August (1-1.5 m) and the decayed and melting FYI closer to the
403 margins in September (<1 m). However, the slope between CryoSat-2 and air EM sea ice thickness measurements
404 is 0.72, so CryoSat-2 does not quite match the full dynamic range of thickness acquired by the helicopter.

405 The CryoSat-2 observations from 2016-2018 underestimate the AEM sea ice thickness observations collected on
406 IceBird campaigns, with a median difference of 28 cm (Extended Data Fig. 3). However, by calculating the
407 CryoSat-2 sea ice thickness without correcting for the roughness induced EM range bias, the median difference
408 increases to 82 cm. The EM range bias for CryoSat-2 is highest over the roughest sea ice in the Lincoln Sea and
409 above Northern Greenland, so it is most crucial to apply a correction in this region. There is a clear relationship
410 between the mean CryoSat-2 and AEM ice thickness difference and the distance from the nearest coastline
411 (Extended Data Fig. 3c). CryoSat-2 underestimates the AEM ice thickness most severely within 150 km of the
412 coast, whereas there is a very low mean difference at distances >150 km from the coastline. This suggests there is
413 still a roughness bias remaining for the heavily deformed sea ice in coastal locations.

414 *Upward Looking Sonar Data*

415 The BGEP moorings have been maintained in the Beaufort Sea since 2003, monitoring freshwater and heat content
416 in the Arctic Ocean including the solid freshwater flux through observations of sea ice draft. ULS ice draft
417 observations from Moorings A, B and D are available here <https://www.whoi.edu/beaufortgyre> for the period
418 between 2011 and 2018 coinciding with our CryoSat-2 sea ice thickness observations. Furthermore, ULS and
419 ADCP ice draft observations have been acquired at five moorings operated by AWI on the opposite side of the
420 Arctic, in the Laptev Sea, and are publicly available here <https://doi.pangaea.de/10.1594/PANGAEA.899275> and
421 <https://doi.pangaea.de/10.1594/PANGAEA.912927>. Four of these moorings are located far enough away from the
422 coast, with data acquired between 2010 and 2016, to be compared with CryoSat-2 sea ice thickness observations
423 ⁶⁷. Each ULS ice draft observation is estimated to have an uncertainty of ± 0.05 - 0.10 m ⁶⁸ whereas each ADCP ice
424 draft is estimated to have a much higher uncertainty of around ± 0.95 m ⁶⁹; however, the uncertainties are reduced
425 by averaging data over time. Finally, ULS ice draft observations have been acquired at four moorings in Fram
426 Strait from 1990 to 2018 and monthly averages are publicly available here
427 <https://doi.org/10.21334/npolar.2021.5b717274>. The comparisons with CryoSat-2 enable us to validate the
428 magnitude and timing of sea ice melting rates obtained from our new year-round SIT product.

429 The sea ice drafts are obtained from CryoSat-2 thickness data by removing the ice freeboard. Satellite-derived ice
430 drafts from a radius of 150 km around each mooring are compared against a 31-day rolling average of daily
431 measurements of the mean ice draft from the mooring ULS and ADCP sensors in Extended Data Figures 4 and 5.

432 The mean bias and standard deviation on the bias are -16 ± 32 cm, -19 ± 34 cm, and -27 ± 42 cm, for BGEP
433 Moorings A, B and D, respectively (CryoSat-2 minus ULS). Notably, the slope of the CryoSat-2-ULS comparison
434 of 0.69 is very similar to the slope on the CryoSat-2-AEM comparisons made for TransArc (Extended Data Fig.
435 2). The correlations between the CryoSat-2 and ULS observations are 0.87, 0.84 and 0.85 for Moorings A, B and
436 D, respectively. If we just use a simple sea ice density-dependent freeboard to draft conversion, and a relatively
437 high sea ice density of 930 kg m^{-3} , without correcting for the EM range bias on freeboards or for snow loading,
438 the correlation is only 0.66 and mean difference is -26 ± 50 cm⁸. By accounting for the range bias and snow
439 loading in the ice freeboard to draft conversion, in this study, the correlation is improved by 30%, offset is reduced
440 by 23%, and variability reduced by 28%. The validity of our corrections for the EM range bias and snow loading
441 are strongly supported by these improved validation statistics.

442 The mean bias and standard deviation on the bias are -6 ± 40 cm for the Laptev Sea Moorings (CryoSat-2 minus
443 ULS/ADCP). The average correlation between the CryoSat-2 and ULS/ADCP observations is 0.74. It is notable
444 that mooring observations from the central Laptev Sea (Kotelny, Outer Shelf, and 1893) match the CryoSat-2 SIT
445 observations better than those from the western Laptev Sea (Vilk) (Extended Data Fig. 5). The central sites are
446 less influenced by dynamics and sea ice deformation, meaning that the ice cover is consistent and the higher
447 uncertainty ADCP observations therefore have less impact. A previous comparison of these observations with a
448 different CryoSat-2 SIT product for only winter months found greater mismatch when the mean and modal ice
449 drafts were very different⁶⁷, which is a sign of strong ice deformation. This is the case for Vilk1 and Vilk3 in 2016
450 when the seasonal cycle of sea ice thickness had a very unusual shape (Extended Data Fig. 5).

451 The mean bias is +11 cm for the Fram Strait Moorings (CryoSat-2 minus ULS) when including all valid
452 observations from winter and summer months. However, the CryoSat-2 ice draft estimates are not available when
453 sea ice concentrations are below 70% which is often the case over the Fram Strait moorings during summer.
454 Therefore, we cannot reliably use the Fram Strait ULS data for validating the new CryoSat-2 summer SIT product.

455 **Sea ice volume**

456 Before estimating sea ice volume from the CryoSat-2 summer ice thickness observations, we fill spatial gaps in
457 the thickness fields (where no valid CryoSat-2 freeboard observations are available) by two methods. Within the
458 marginal ice zone (MIZ), which is here defined as the area with sea ice concentration $>15\%$ and $<60\%$, grid cells
459 missing valid freeboard observations but containing strongly specular radar returns are assumed to characterize
460 mainly thin, heavily pond-covered, and decayed sea ice floes²¹. These grid cells are defined where the backscatter
461 coefficient >40 dB, the range integrated power (RIP) peakiness⁸ >25 , or the pulse peakiness >0.3 . To these cells
462 we assign a thickness from the 5th percentile of the pan-Arctic ice thickness distribution for that time interval and
463 an uncertainty of 50%. We use this method because the thickness in these marginal grid cells cannot be reliably
464 interpolated from adjacent cells which may contain much thicker ice. However, only a small number of gaps are
465 filled in this way, for instance 4-5 grid cells per biweekly time slice in 2016. Remaining gaps within the main ice

466 pack (ice concentrations >60%) are filled via linear interpolation from up to eight adjacent grid cells. (N.B. the
467 data product provided with this paper includes two thickness fields both omitting and including these gap-filled
468 grid cells).

469 Sea ice volume is then obtained from the ice thickness grids multiplied by sea ice concentration from the OSISAF
470 ‘OSI-450’ climate data record (available from <https://osi-saf.eumetsat.int/products/osi-450>⁷⁰) and the grid cell
471 area. CryoSat-2-derived SIV is compared to the Applied Physics Laboratory Version 2.1 reprocessed PIOMAS
472 ice volume data^{9,31}, using the NSIDC Sea ice Age, Version 4 dataset⁴³ to separate zones of predominantly FYI and
473 MYI. The domains are matched by comparing gridded SIV observations to the native PIOMAS grid and removing
474 all non-overlapping data. Sea ice volume anomalies, SIV’, are obtained from the time series of pan-Arctic SIV by
475 removing the 2010-2020 climatological seasonal cycle. The SIV anomalies are decomposed as follows

$$SIV' = \int_A (SIC' \overline{SIT} + \overline{SIC} SIT' + SIC' SIT') dA \quad (5)$$

476 where bars represent the climatology and primes the anomalies of SIC and SIT, and A represents the area. We
477 confirm that SIT anomalies provide approximately five times the absolute contribution to interannual variability
478 of SIV than SIC anomalies do (Extended Data Fig. 7).

479 **Lagged correlation analysis with sea ice volume and extent**

480 We calculate the lagged Pearson product moment correlation coefficient between 9–11-year time series of
481 biweekly CryoSat-2 SIV and future daily pan-Arctic SIE from OSI-450, up to a maximum lead time of 365 days.
482 Only the SIV observations from outside the NSIDC Multisensor Analyzed Sea Ice Extent (MASIE) Central Arctic
483 region⁷¹ are used for these calculations because the Central Arctic was perennially sea ice covered over our study
484 period. (It is important to note this region should be included in a similar analysis if the Central Arctic sea ice
485 coverage varies between seasons, for instance in a model analysis of future SIV and SIE fields.) We compare this
486 to lagged correlations between biweekly SIE and future daily SIE. Only 1 of the 24 biweekly (i.e., twice monthly
487 for a year) pan-Arctic SIV fields, and 6 of the 24 SIE fields, exhibit statistically significant ($p < 0.05$) trends over
488 the 2011-2020 study period. Therefore, we show correlations without detrending in the main paper but repeat the
489 same analysis with detrended time series in Extended Data Figure 8. The given p -values for correlations are based
490 on an F test. Although SIE is available daily, SIV is available at biweekly intervals, so correlations can only be
491 obtained for select lead day-target day pairs. To visualize the correlation maps we use a two-dimensional median
492 filter (with a radius of 21 days) to interpolate between gaps. Correlation maps for eight regions based on the MASIE
493 definitions⁷¹ are also shown in Extended Data Figure 9.

494 Significant correlations can be obtained between the ‘radar freeboard volume’ (the original uncorrected CryoSat-
495 2 radar freeboards multiplied by the sea ice area) and the future pan-Arctic SIE. However, replacing corrected sea
496 ice volume (Fig. 3a) with uncorrected radar freeboard volume results in approximately half the increase in lead
497 time of skilful September sea ice forecasts, versus the reference forecast using sea ice extent (Fig. 3b). This

498 emphasizes the importance of the freeboard to thickness conversion in summer (freeboard bias correction and
499 impact of snow load) and in winter (impact of snow load only) for improving seasonal predictions.

500 A bootstrapping approach is used to assess the robustness of correlations. The correlations cover a period of 9-11
501 years depending on the availability of CryoSat-2 observations for a certain target day and lead time. So, the above
502 analysis is repeated 100 times but randomly sampling all but one year of the 9-11-year time series, with
503 replacement, to determine the standard deviation (variability) of the correlations. In Extended Data Figure 10, the
504 variability of the 100 recalculated correlation coefficients provides a measure of the robustness of the patterns
505 identified in Figure 3 of the main paper. Extended Data Figure 10 also shows the same bootstrapping analysis for
506 the detrended correlation maps in Extended Data Figure 8. For the regions of SIE correlations at lead times up to
507 3 months, using either SIV or SIE, the standard deviations of the bootstrapped correlations are generally <0.06
508 (and <0.04 for target days in September). However, the re-emergence region of sea ice correlations for SIV leading
509 SIE, at 100-280 days for target days in October-November, produces standard deviations on the bootstrapped
510 correlations of 0.06-0.10 (Extended Data Fig. 10). We require a longer consistent time series of sea ice thickness
511 observations to more robustly validate this re-emergence region of correlations based on SIV anomalies.

512

513 **Data availability**

514 ESA Level-2 Baseline-D CryoSat-2 observations for May-September 2011-2020 from the ESA Grid Processing
515 On Demand (GPOD) *SARvatore* and *SARInvatore* services were publicly available online for the initial manuscript
516 submission but have since been removed. Please contact the lead author directly for access to these data. The
517 dataset of samples for training and testing the CNN classification algorithm for CryoSat-2 is available from
518 <https://doi.org/10.1016/j.rse.2021.112744>⁸. Daily observations of sea ice drift are available from the NSIDC Polar
519 Pathfinder dataset <https://nsidc.org/data/nsidc-0116/versions/4>⁴³. Remotely sensed observations of melt pond
520 fraction are available from the Sentinel-3 OLCI sensor through the University of Bremen [https://seaice.uni-
521 bremen.de/melt-ponds/](https://seaice.uni-bremen.de/melt-ponds/)⁵⁴. Snow depth and density estimates from SnowModel-LG are available from NSIDC
522 <https://doi.org/10.5067/27A0P5M6LZBI>²⁶. Weekly 12.5 km estimates of the sea ice age are available from the
523 Version 4 product at NSIDC <https://nsidc.org/data/nsidc-0611>⁷². The Airborne EM dataset includes observations
524 from the AWI Polarstern ARK-XXVI/3 *TransArc* campaign in 2011⁶⁴, available from
525 <https://doi.org/10.1594/PANGAEA.937197>, and the *IceBird* campaigns from 2016 to 2018²³. Daily ULS sea ice
526 draft observations from BGEP Moorings A, B and D are available from <https://www.whoi.edu/beaufortgyre>
527 for the period between 2011 and 2018. Daily ULS and ADCP ice draft observations from five moorings in the Laptev
528 Sea for 2010 to 2016 are publicly available from <https://doi.pangaea.de/10.1594/PANGAEA.899275> and
529 <https://doi.pangaea.de/10.1594/PANGAEA.912927>. Monthly ULS ice draft observations from four moorings in
530 Fram Strait between 2010 and 2018 are publicly available from <https://doi.org/10.21334/npolar.2021.5b717274>.

531 Sea ice concentration is available from the OSISAF ‘OSI-450’ climate data record at <https://osisaf.eumetsat.int/products/osi-450>⁷⁰. Reanalysed model estimates of sea ice volume are available from the Applied
532 Physics Laboratory Version 2.1 reprocessed Pan-Arctic Ice Ocean Modeling and Assimilation System (PIOMAS)
533 ^{9,31} at http://psc.apl.uw.edu/research/projects/arctic-sea-ice-volume-anomaly/data/model_grid. The final pan-
534 Arctic CryoSat-2 sea ice thickness data spanning October 2010 to July 2020 are available from the British
535 Antarctic Survey Polar Data Centre at <https://doi.org/10.5285/D8C66670-57AD-44FC-8FEF-942A46734ECB>.

537 Code availability

538 The *MATLAB* Facet-Based Echo Model (FBEM) for simulating the backscattered SAR altimeter waveform from
539 snow-covered sea ice, including an option for simulating waveforms from melt-pond covered sea ice, is publicly
540 available at <https://doi.org/10.5281/zenodo.6554740>. The lookup table for the EM bias correction is available at
541 <https://doi.org/10.5281/zenodo.6558485>. The code for converting CryoSat-2 radar freeboards to thickness is
542 available at <https://doi.org/10.5281/zenodo.6558483>.

543

42. Landy, J. C., Petty, A. A., Tsamados, M. & Stroeve, J. C., Sea ice roughness overlooked as a key source of uncertainty in CryoSat-2 ice freeboard retrievals. *J. Geophys. Res. Oceans* **125**, e2019JC015820 (2020).
43. Tschudi, M., Meier, W. N., Stewart, J. S., Fowler, C. & Maslanik, J. (NASA National Snow and Ice Data Center Distributed Active Archive Center, Boulder, Colorado, USA, 2019).
44. Wingham, D. J. *et al.*, CryoSat: A mission to determine the fluctuations in Earth’s land and marine ice fields. *Adv. Space Res.* **37** (4), 841-871 (2006).
45. Dinardo, S. *et al.*, Coastal SAR and PLRM altimetry in german bight and west baltic sea. *Adv. Space Sci.* **62** (6), 1371-1404 (2018).
46. Landy, J. C., Tsamados, M. & Scharien, R. K., A Facet-Based Numerical Model for Simulating SAR Altimeter Echoes from Heterogeneous Sea Ice Surfaces. *IEEE Trans. Geosci. Rem. Sens.* **57** (7), 4164-4180 (2019).
47. Kurtz, N. T., Galin, N. & Studinger, M., An improved CryoSat-2 sea ice freeboard retrieval algorithm through the use of waveform fitting. *Cryosphere* **8**, 1217-1237 (2014).
48. Polashenski, C., Perovich, D. & Courville, Z., The mechanisms of sea ice melt pond formation and evolution. *J. Geophys. Res.* **117**, C01001 (2012).
49. Fetterer, F. M., Drinkwater, M. R., Jezek, K. C., Laxon, S. W. & Onstott, R. G., in *Microwave Remote Sensing of Sea Ice*, edited by Carsey, F. (American Geophysical Union, Washington D.C., 1992), pp. 111-135.
50. Fung, A. K. & Chen, K. S., An update on the IEM surface backscattering model. *IEEE Geosci. Rem. Sens. Lett.* **1** (2), 75-77 (2004).
51. Ray, C. *et al.*, SAR altimeter backscattered waveform model. *IEEE Trans. Geosci. Rem. Sens.* **53** (2), 911-919 (2015).
52. Ulaby, F. T., Moore, R. K. & Fung, A. K., *Microwave Remote Sensing: Active and Passive* (Artech House, Boston, MA, 1982).
53. Scharien, R. K., Landy, J. & Barber, D. G., First-year sea ice melt pond fraction estimation from dual-polarisation C-band SAR—Part 1: In situ observations. *The Cryosphere* **8** (6), 2147-2162 (2014).
54. Istomina, L. *et al.*, *Retrieval of sea ice surface melt using OLCI data onboard Sentinel-3*, presented at AGU Fall Meeting, San Francisco, 2020 (unpublished).
55. Landy, J. C., Ehn, J. K. & Barber, D. G., Albedo feedback enhanced by smoother Arctic sea ice. *Geophys. Res. Lett.* **42** (24), 10714-10720 (2015).
56. Landy, J., Ehn, J., Shields, M. & Barber, D., Surface and melt pond evolution on landfast first-year sea ice in the Canadian Arctic Archipelago. *J. Geophys. Res.* **119**, 3054-3075 (2014).

57. Willatt, R. C., Giles, K. A., Laxon, S. W., Stone-Drake, L. & Worby, A. P., Field investigations of Ku-band radar penetration into snow cover on Antarctic sea ice. *IEEE Trans. Geosci. Rem. Sens.* **48** (1), 365-372 (2009).
58. Willatt, R. *et al.*, Ku-band radar penetration into snow cover on Arctic sea ice using airborne data. *Ann. Glaciol.* **52** (57), 197-205 (2011).
59. Nandan, V. *et al.*, Effect of Snow Salinity on CryoSat-2 Arctic First-Year Sea Ice Freeboard Measurements. *Geophys. Res. Lett.* **44** (20), 10419–10426 (2017).
60. Stroeve, J. *et al.*, Surface-based Ku-and Ka-band polarimetric radar for sea ice studies. *Cryos.* **14** (12), 4405-4426 (2020).
61. Mallett, R. D., Lawrence, I. R., Stroeve, J. C., Landy, J. C. & Tsamados, M., Brief communication: Conventional assumptions involving the speed of radar waves in snow introduce systematic underestimates to sea ice thickness and seasonal growth rate estimates. *Cryosphere* **14** (1), 251-260 (2020).
62. Alexandrov, V., Sandven, S., Wahlin, J. & Johannessen, O. M., The relation between sea ice thickness and freeboard in the Arctic. *Cryosphere* **4** (3), 373-380 (2010).
63. Ricker, R., Hendricks, S., Helm, V., Skourup, H. & Davidson, M., Sensitivity of CryoSat-2 Arctic sea-ice freeboard and thickness on radar-waveform interpretation. *Cryosphere* **8**, 1607-1622 (2014).
64. Hendricks, S. *et al.* (PANGAEA, Alfred Wegener Institute, Helmholtz Centre for Polar and Marine Research, Bremerhaven, 2012).
65. Pfaffling, A., Haas, C. & Reid, J., A direct helicopter EM sea ice thickness inversion, assessed with synthetic and field data. *Geophys.* **72**, 127-137 (2007).
66. Haas, C., Gerland, S., Eicken, H. & Miller, H., Comparison of sea-ice thickness measurements under summer and winter conditions in the Arctic using a small electromagnetic induction device. *Geophys.* **62** (3), 749-757 (1997).
67. Belter, H. J. *et al.*, Satellite-based sea ice thickness changes in the Laptev Sea from 2002 to 2017: comparison to mooring observations. *Cryosphere* **14**, 2189–2203 (2020).
68. Krishfield, R. A. & Proshutinsky, A., BGOS ULS Data Processing Procedure. *Woods Hole Oceanographic Institute report* (1 Sept 2021) (2006).
69. Belter, H. J., Krumpen, T., Janout, M. A., Ross, E. & Haas, C., An Adaptive Approach to Derive Sea Ice Draft from Upward-Looking Acoustic Doppler Current Profilers (ADCPs), Validated by Upward-Looking Sonar (ULS) Data. *Rem. Sens.* **13** (21), 4335 (2021).
70. Lavergne, T. *et al.*, Version 2 of the EUMETSAT OSI SAF and ESA CCI sea-ice concentration climate data records. *Cryosphere* **13** (1), 49-78 (2019).
71. Fetterer, F., Savoie, M., Helfrich, S. & Clemente-Colón, P., Multisensor Analyzed Sea Ice Extent - Northern Hemisphere (MASIE-NH), Version 1. *National Snow and Ice Data Centre, Boulder, Colorado USA* (September 2021) (2010).
72. Tschudi, M., Meier, W. N., Stewart, J. S., Fowler, C. & Maslanik, J. (NASA National Snow and Ice Data Center Distributed Active Archive Center, Boulder, Colorado USA, 2019).

545

546 **Acknowledgements**

547 M.T., J.L., Y.A., G.D., J.S. and H.H. acknowledge financial support from the UKRI Natural Environment Research
548 Council Project (NERC) “PRE-MELT” under the split grant awards NE/T001399/1, NE/T000546/1 and
549 NE/T000260/1. J.L. was also supported by the European Space Agency Living Planet Fellowship “Arctic-
550 SummIT” under Grant ESA/4000125582/18/I-NS and the CIRFA project through the Research Council of Norway
551 (RCN) under Grant #237906. D.B. acknowledges support from the Natural Sciences and Engineering Research
552 Council of Canada (NSERC). M.T. and Y.A. acknowledge support from “Towards a marginal Arctic sea ice cover”
553 (NE/R000085/1). The authors thank the SARvatore (SAR Versatile Altimetric Toolkit for Ocean Research &
554 Exploitation) service available through ESA Grid Processing on Demand (GPOD) for providing Level 2 CryoSat-
555 2 observations. We further thank the WHOI Beaufort Gyre Exploration Programme and AWI IceBird Programme
556 for providing essential observations for ground truthing new satellite datasets. ADCP and ULS Moorings were

557 deployed, recovered and processed within the framework of the Russian-German project CATS/Transdrift (grant:
558 63A0028B) and QUARCCS (grant: 03F0777A).

559 **Author Contributions**

560 J.L. conceived the study and managed the research. M.T., J.L. and Y.A. wrote the grant proposals that majority
561 funded the study. J.L., G.D., J.S., S.H., T.K., H.B. and A.K. collected and prepared the raw data. J.L and G.D.
562 developed the methods and wrote the software. M.B. and J.L. designed the lagged correlation analyses. J.L. led
563 the writing of the paper and produced the figures. All authors revised and improved the manuscript.

564 **Author Information**

565 Requests for reprints, permissions and other correspondence should be addressed to Jack Landy,
566 jack.c.landy@uit.no. The authors have no financial or non-financial competing interests.